Materials Science & Engineering A 836 (2022) 142711

Contents lists available at ScienceDirect

Materials Science & Engineering A

journal homepage: www.elsevier.com/locate/msea

Crack initiation and propagation behaviour under high-temperature very-high-cycle fatigue: Directionally solidified columnar-grained vs. single-crystal superalloys

Z. Zhao [a,**], Z. Liang [a], Q. Li [b], F. Zhang [b], B. Chen [c,*]

[a] School of Materials Science and Engineering, Beihang University, Beijing, 100191, China
[b] School of Energy and Power Engineering, Beihang University, Beijing, 100191, China
[c] School of Engineering, University of Leicester, Leicester, LE1 7RH, UK

ARTICLE INFO

Keywords:
High-temperature fatigue
Very high cycle fatigue
Oxidation
Single crystal
Directionally solidified
Ni-base superalloy

ABSTRACT

Role of oxidation and recrystallisation on very-high-cycle fatigue of columnar-grained DZ125 and single-crystal DD6 superalloys are investigated. With the temperature increase from 850 to 1000 °C for DZ125 while from 1000 to 1100 °C for DD6, the Mode-I cracking tendency increases due to internal oxide penetration. Recrystallisation can occur for both the electrolytically and mechanically polished surface conditions, controlled primarily by temperature and test duration. Its presence can lead to strain localisation at subsurface, but the surface recrystallisation does not necessarily determine the oxide penetration. By comparison with the single-crystal DD6 that shows the pure Stage I at 1000 °C, the columnar-grained DZ125 exhibits the distinctive Stage I cracking followed by Mode I propagation. This fracture characteristics in DZ125 can be attributed to the combined effect of the high-angle grain boundaries and far-field stress. The microstructure-related factor plays a vital role when the crack length is small, whereas the role of stress becomes predominant when the crack length is comparable to a couple of grains, ultimately leading to the shift from the crystallographic Stage I to Mode I propagation.

1. Introduction

Very-high-cycle fatigue (VHCF) at elevated temperature has been studied on Ni-base superalloys in the form of single-crystal [1–9], columnar-grained [4,10], and polycrystal [11], with a large amount of fatigue data suggesting endurance limit defined at 10^7 fatigue cycles might not hold true [1–4,10]. Within this group, the single-crystal and columnar-grained superalloys including CMSX-4 and CMSX-4 Plus [4–9], PWA1484 [1,2], Mar-M200 + Hf and its columnar-grained version of DS200 + Hf [4], DZ125 [10], DD6 [3], CM186LC [6] and TMS138A [7], have been tested in the temperature range of 600–1100 °C. Compared with the single crystal, limited work was performed on the columnar-grained superalloy in the VHCF regime at high temperature.

Based on three VHCF tests, Cervellon et al. [4] observed little difference in the VHCF lifetime at 1000 °C by comparing the DS200 + Hf with many single-crystal superalloys. They also commented on the fatal-crack initiation mode transition from crystallographic Stage I (along {111} slip planes), associated with either casting pore or a cluster of carbides, to Mode I (perpendicular to the far-field applied stress), arising from surface oxides and interrupted by grain boundary. Zhao et al. [10] performed thirty-six VHCF tests on columnar-grained DZ125 alloy up to 850 °C. Crystallographic Stage I cracking initiated primarily from the casting pore. The selected temperature of 850 °C in Ref. [10] apparently does not allow understanding the role of oxidation.

Therefore, the present work is aimed to unravel the controlling mechanisms of the crack initiation mode transition and subsequent propagation in columnar-grained Ni-base superalloy. This goal is achieved by conducting a large number of VHCF tests on DZ125 alloy at 1000 °C, followed by examining the fractography and microstructure. Additional 850 °C tests are included for a twofold reason: first, corroborating the data consistency with the previous work [10] and, second, permitting the data comparison with 1000 °C tests.

In terms of the fatal-crack initiation mode transition in the high-temperature VHCF regime (10^6 to 10^9 cycles), nearly all studies were performed on the single-crystal superalloys. Yi et al. [2] found that one

* Corresponding author.
** Corresponding author.
E-mail addresses: zhzh@buaa.edu.cn (Z. Zhao), bo.chen@leicester.ac.uk (B. Chen).

https://doi.org/10.1016/j.msea.2022.142711
Received 5 October 2021; Received in revised form 23 December 2021; Accepted 19 January 2022
Available online 22 January 2022

Table 1
Chemical compositions of the DD6 and DZ125 alloys (in wt.%) with Ni in balance.

Alloy	C	Cr	Co	Mo	W	Ta	Ti	Al	B	Hf	Re	Nb
DZ125	0.1	9.0	10.0	2.1	7.1	3.8	1.0	5.2	0.02	1.6	N/A	N/A
DD6	0.04	4.3	9.0	2.0	8.0	7.5	0.1	5.6	0.02	0.1	2.0	0.5

out of six specimens made of PWA1484 fatigued at 1000 °C exhibited a surface oxide layer with thickness of 20–30 μm. However, the oxidation induced cracks did not lead to the fatal-crack initiation. In a later work on CMSX-4 at 1000 °C [5], neither the prolonged test duration of 10^{10} cycles, nor coarsened γ′-microstructure induced by pre-ageing, can trigger any measurable oxidation effect on fatal-crack initiation. But, it was commented in Ref. [4] that at long lifetimes, a competition occurred between the internal and surface initiation modes, although no evidence was provided. The high-cycle fatigue work on CMSX-4 Plus found the fatal-crack initiation from oxide layer and high sensitivity of microstructure to recrystallisation at 950 °C [9]. Unfortunately, no detailed characterisation was performed to reach unambiguous conclusion.

Our previous VHCF work [3] on single-crystal DD6 identified that the fatal-crack initiation can switch to Mode I at 1100 °C with enhanced oxidation, when compared to that of 1000 °C characterised by the Stage I cracking. But, the role of surface finish and associated recrystallisation remains unclear. This seems to be important as the conditions that trigger the crack initiation mode transition, primarily during the low-cycle fatigue, are related to either the recrystallised grains [12], oxidation [13–15], or perhaps their combination.

Therefore, the accompanying aim of the present study is to critically assess the individual role of surface recrystallisation and oxidation on the VHCF behaviour. Also, the comparative study of columnar-grained DZ125 and single-crystal DD6 in the high-temperature VHCF regime holds the promise in elucidating the role of grain boundary in conjunction with carbides on fatigue cracking.

2. Material and experimental

2.1. Ni-base superalloys

DZ125 has been selected as the columnar-grained Ni-base superalloy, while DD6 as the single-crystal one. Both superalloys were processed by directional solidification technique. Their chemical compositions are given in Table 1. Two distinct differences deserve particular attention: first, DZ125 contains high Hf and C, thereby promoting the formation of Hf-rich MC carbides [16]; second, high Cr and Ti in DZ125 were found to create complex oxide scales [17]. Both alloys were supplied in a bar shape with 15 mm in diameter.

The DZ125 alloy was solution treated at 1180 °C/2 h + 1230 °C/3 h, and then precipitate aged at 1100 °C/4 h + 870 °C/20 h. The resulting microstructure is characterised by the grain width of 883.3 ± 40.5 μm, primary dendrite spacing of 202.5 ± 23.6 μm, γ′-volume fraction of 60.0%, edge length of 0.45 ± 0.09 μm and γ-channel width of 0.07 ± 0.02 μm. The DD6 alloy was subjected to solution treating at 1290 °C/1 h + 1300 °C/2 h + 1315 °C/4 h, and precipitate ageing at 1120 °C/4 h + 870 °C/32 h. The microstructure is characterised by the primary dendrite spacing of 242.8 ± 29.4 μm, γ′-volume fraction of 70.2%, edge length of 0.36 ± 0.12 μm and γ-channel width of 0.06 ± 0.01 μm.

2.2. Very-high-cycle fatigue (VHCF)

High-temperature VHCF tests were conducted using a Shimadzu USF-2000 ultrasonic instrument operating at 20 ± 0.5 kHz. A fully reversed fatigue loading was used, namely, at the stress ratio of $R = -1$. The loading axis was parallel to the [001] direction. For the DZ125, tests were performed at 850 and 1000 °C with stress amplitudes ranging from 215 to 350 MPa. By comparison, tests on DD6 were performed at 1000 and 1100 °C with stress amplitudes from 175 to 250 MPa. The VHCF specimen dimension of the 1000 °C DZ125 is shown in Fig. 1, while the others can be found in Refs. [3,10]. Using the dynamic elastic modulus of $E_d = 84$ GPa, the specimen was designed with a total length of 40 mm within the varying cross section, end length of 6 mm, the minimum diameter of 5 mm and maximum diameter of 10 mm.

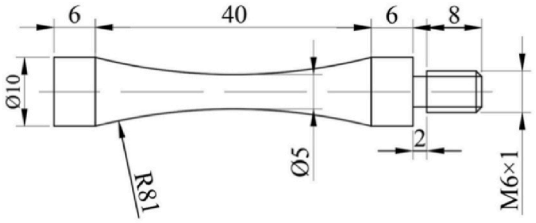

Fig. 1. 1000 °C VHCF specimen dimension for DZ125 alloy.

Prior to the VHCF loading, a 20 min thermal exposure at the test temperature was applied to achieve a uniform temperature and form a stabilised oxide layer. To limit the specimen self-heating, intermittent excitation mode was used. All the pulse/pause conditions were recorded and summarised in Table S1. One should bear in mind that the pulse/pause loading procedure affects the total test duration, potentially altering the effect of oxidation. But according to the present data, no systematic effect induced by applying different pulse/pause conditions was found.

The majority of DZ125 specimens were mechanically polished down to a 5000-grit surface finish, except for two 1000 °C specimens that received a further electrolytic polishing. In terms of the DD6, all 1100 °C and most of the 1000 °C specimens had the electrolytic polishing. The polishing was conducted in a solution of 20 vol% $HClO_4$ and 80 vol% C_2H_6O at 0 °C using 27 V for 15s. The surface finish condition will be specified wherever relevant. The selected test temperatures (850 and 1000 °C for DZ125, while 1000 and 1100 °C for DD6) accounted for the material's intrinsic susceptibility to recrystallisation and oxidation.

2.3. Post-mortem examination

A Zeiss Supra-55 field-emission-gun scanning electron microscope (SEM) was used to perform the fractographic examination on all VHCF specimens to identify the crack initiation and propagation characteristics. This was followed by performing the longitudinal cross-section on selected specimens to aid the interpretation of failure mechanisms. The cross-section was prepared close to the fatal-crack initiation region, and the metallographic sample preparation was either down to the mechanically polished or etched condition, depending on the feature of interest (i.e. crack morphology or γ/γ′-microstructure). Chemical etching was conducted using a solution containing 5 g $CuSO_4$, 15 mL HCl and 25 mL H_2O to preferentially dissolve the γ′-precipitate, thereby leaving the γ-phase in the micrograph. Energy-dispersive X-ray spectrometry (EDS) was used to identify carbides and oxides.

A Tescan Mira3 SEM equipped with the electron backscatter diffraction (EBSD) detector was used to study the recrystallisation, local misorientation, grain orientation and phase identification. EBSD scans were collected at 20 kV using step sizes ranging from 0.15 to 3 μm, and data post-processing was performed using the HKL Channel 5. Sample preparation involved grinding down to 2000-grit, polishing down to 1 μm, and finally OPS polishing with 0.05 μm colloidal silica to achieve the deformation-free surface [18].

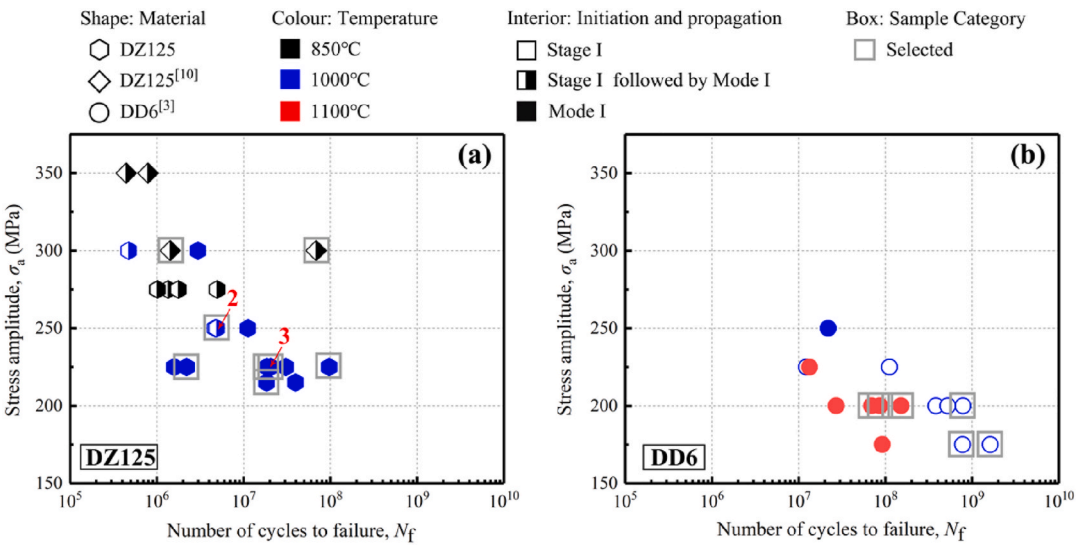

Fig. 2. Fatigue S–N data: (a) columnar-grained DZ125 alloy at 850 and 1000 °C; (b) single-crystal DD6 alloy at 1000 and 1100 °C. Different colours indicate temperature levels, while the filled, partially filled and empty shapes indicate different failure modes as identified from the SEM fractography. (For interpretation of the references to colour in this figure legend, the reader is referred to the Web version of this article.)

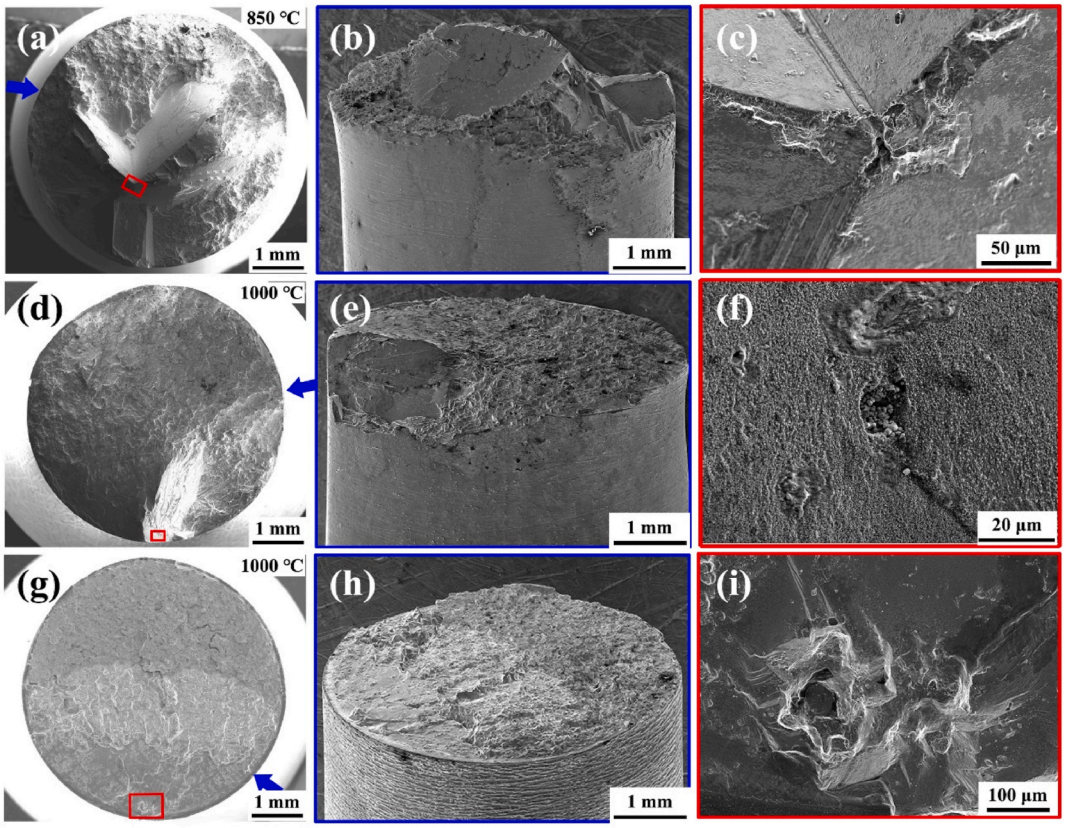

Fig. 3. SEM fractography of DZ125 specimens tested at 850 and 1000 °C: (a) to (c) $\sigma_a = 300$ MPa, $N_f = 1.43 \times 10^6$, 850 °C; (d) to (f) $\sigma_a = 225$ MPa, $N_f = 2.04 \times 10^7$, 1000 °C; (g) to (h) $\sigma_a = 225$ MPa, $N_f = 1.85 \times 10^7$, 1000 °C. (a), (d) and (g) are the top view with the red box indicating the enlarged views of the fatal-crack initiation site as presented in (c), (f) and (i). (b), (e) and (h) are the side view of the fracture surface with the viewing direction indicated by the blue arrow. All three specimens had the mechanically polished surface condition. (For interpretation of the references to colour in this figure legend, the reader is referred to the Web version of this article.)

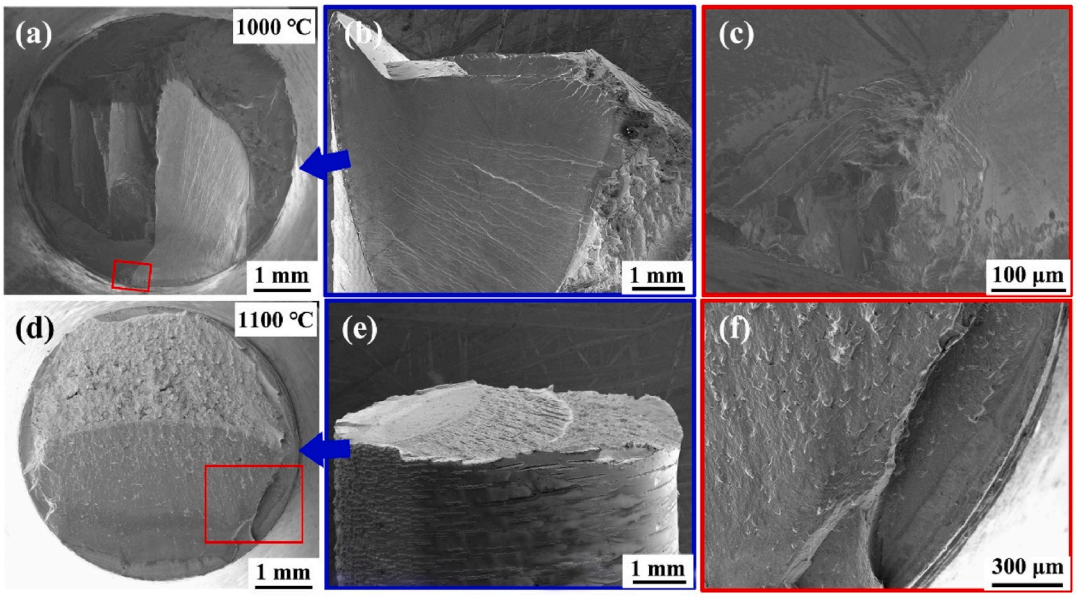

Fig. 4. SEM fractography of DD6 tested at 1000 and 1100 °C: (a) to (c) mechanically polished, $\sigma_a = 200$ MPa, $N_f = 7.86 \times 10^8$, 1000 °C; (d) to (f) electrolytically polished, $\sigma_a = 200$ MPa, $N_f = 6.95 \times 10^7$, 1100 °C. Note: the red box in (a) indicates a subsurface crack initiation, instead of surface initiation, and its enlarged view is given in (c). (For interpretation of the references to colour in this figure legend, the reader is referred to the Web version of this article.)

3. Results

3.1. Fatigue S–N diagrams

In general, the fatigue life, N_f, increased with the decreasing stress amplitude, σ_a, for the DZ125 alloy (Fig. 2a), and this trend applies to both the 1000 °C and 850 °C. Some of the data points overlapped with each other due to the similar cycles to failure (Table S1). The number of tests is indicated beside those data points in Fig. 2a. At 1000 °C, the DZ125 exhibited two distinct fracture modes including Mode I cracking (filled shape in Fig. 2a) and Stage I cracking followed by Mode I propagation (partially filled shape in Fig. 2a). The specimen characterised by the Mode I cracking accounted for 64.3% (9 out of the 14 tested specimens). As a comparison, all specimens tested at 850 °C exhibited the characteristic Stage I cracking followed by Mode I propagation. For the single-crystal DD6 at 1000 °C, except for one (Mode I, filled blue circle in Fig. 2b), all the other specimens exhibited the Stage I cracking characteristics (empty blue circle in Fig. 2b). By contrast, all specimens tested at 1100 °C were characterised by the Mode I cracking (filled red circle in Fig. 2b).

3.2. SEM fractography

Representative samples were selected for illustration of the fracture features, as indicated by the box in Fig. 2. For the DZ125 at 850 °C, top view of the fracture surface (Fig. 3a) shows that the fatal fatigue-crack initiated from the interior of the specimen. Together with the side view (Fig. 3b), the cracking behaviour can be described as follows. The fatal-crack initiation and early-stage propagation occurred on the {111} crystallographic plane, followed by transition to Mode I propagation. The Mode I proportion with reference to the total area of fatigue cracking at 850 °C accounted for 58.1% in average with the highest being 82.9% and lowest being 34.4% (all data summarised in Table S2). Note that the final rapid fracture area had not been included in the above-mentioned area analysis. Fig. 3c shows the enlarged view of the initiation area where a casting pore, located at a distance of 1574.3 μm to the specimen surface, is judged to trigger the fatal-crack initiation.

For the DZ125 at 1000 °C, SEM fractographies in Fig. 3d and e were taken from the specimen ($\sigma_a = 225$ MPa, $N_f = 2.04 \times 10^7$) representative of those exhibiting Stage I cracking followed by Mode I propagation (partially filled shape in Fig. 2a), while Fig. 3g and h were taken from the specimen ($\sigma_a = 225$ MPa, $N_f = 1.85 \times 10^7$) with the Mode I cracking (filled shape in Fig. 2a). Note that both specimens had received the mechanical polishing prior to the VHCF test, and thus the different cracking modes cannot be attributed to the electrolytic vs. mechanical polishing.

Oxidation induced cracks appeared at the surface of specimen that exhibited Mode I cracking, see the side view in Fig. 3h. High-magnification SEM in Fig. 3i still revealed an internal casting pore, located at a distance of 250.6 μm to the surface. For the other specimen characterised by the Stage I cracking followed by Mode I propagation, Fig. 3e, the fatal-crack initiation occurred from an internal casting pore, Fig. 3f. In addition, the area proportion of Mode I propagation in those specimens accounted for 77.1% in average with the highest being 87.3% and lowest being 68.6% (Table S2). This suggests that with the temperature increase from 850 to 1000 °C, the DZ125 becomes prone to Mode I cracking. The two competing VHCF crack-initiation mechanisms of defect-dominating internal fatigue vs. surface oxidation seem to be a plausible explanation.

For the DD6, representative SEM fractographies are shown in Fig. 4a–c for the 1000 °C, while in Fig. 4d–f for the 1100 °C specimen. At 1000 °C, the fracture surface was found to be entirely Stage I (excluding the rapid fracture area), Fig. 4a and b. The fatal-crack initiation occurred from the interior, with a distance of 159.7 μm to the surface, Fig. 4c. At 1100 °C, the periphery of the fracture surface was full of the internal oxide penetration, see Fig. 4d for the overall fracture surface and Fig. 4f for a typical oxide penetration and developed crack to a depth of ~500 μm. As a summary, with the temperature increase from 1000 °C to 1100 °C, the DD6 showed a shift towards the Mode I cracking, due to the oxidation. Although other factors such as the plasticity [19] and creep [20,21] can also trigger the Mode I cracking in Ni-base superalloys, they are less likely in the present case, given the test condition of $R = -1$ and 20 kHz frequency.

When compared with the DZ125, there are two primary differences. First, at relatively low temperature, the DZ125 showed Stage I followed by Mode I (850 °C, Fig. 3a and b), but the DD6 showed entirely Stage I cracking (1000 °C, Fig. 4a and b). Second, at relatively high temperature, the DZ125 showed fatigue cracking from casting pore at the micro-

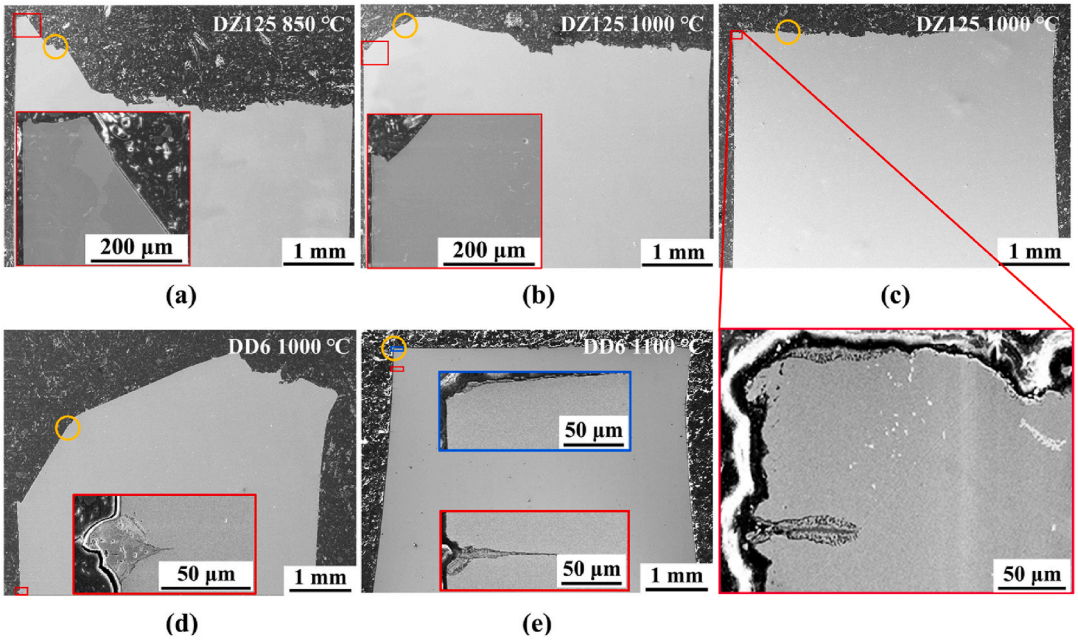

Fig. 5. Cross-sectional SEM observations of the fatal-crack path and subsurface: (a) mechanically polished DZ125, $\sigma_a = 300$ MPa and 850 °C, $N_f = 6.87 \times 10^7$; (b) electrolytically polished DZ125, $\sigma_a = 250$ MPa and 1000 °C, $N_f = 4.91 \times 10^6$; (c) mechanically polished DZ125, $\sigma_a = 225$ MPa and 1000 °C, $N_f = 9.68 \times 10^7$; (d) electrolytically polished DD6, $\sigma_a = 175$ MPa and 1000 °C, $N_f = 7.77 \times 10^8$; (e) electrolytically polished DD6, $\sigma_a = 200$ MPa and 1100 °C, $N_f = 6.95 \times 10^7$. Note: yellow circles indicate the fatal-crack initiation site identified by the SEM fractography. (For interpretation of the references to colour in this figure legend, the reader is referred to the Web version of this article.)

scale (1000 °C, Fig. 3i), but such feature was not observed in the DD6 (1100 °C, Fig. 4f), despite that both materials were fractured by Mode I at the macro-scale.

3.3. Crack initiation mode transition and subsequent propagation

Fig. 5a–c presents the cross-section of the DZ125 fracture surface. At 850 °C, the specimen showed a typical Stage I cracking followed by Mode I propagation, Fig. 5a. The enlarged view of Fig. 5a confirms the absence of oxide penetration at 850 °C. At 1000 °C, the DZ125 specimen failed by the Stage I followed by Mode I (Fig. 5b) exhibited little oxide penetration (the enlarged view of Fig. 5b), whereas the specimen characterised by the Mode I (Fig. 5c) showed clearly the internal oxide penetration and cracking (the enlarged view of Fig. 5c). The oxidised region just beneath the fracture surface, provides unambiguous evidence to indicate the role of oxidation on Mode I cracking. A total of 21 individual cracks associated with the oxide penetration were found within the distance of 1 mm away from the fractured surface. The crack length

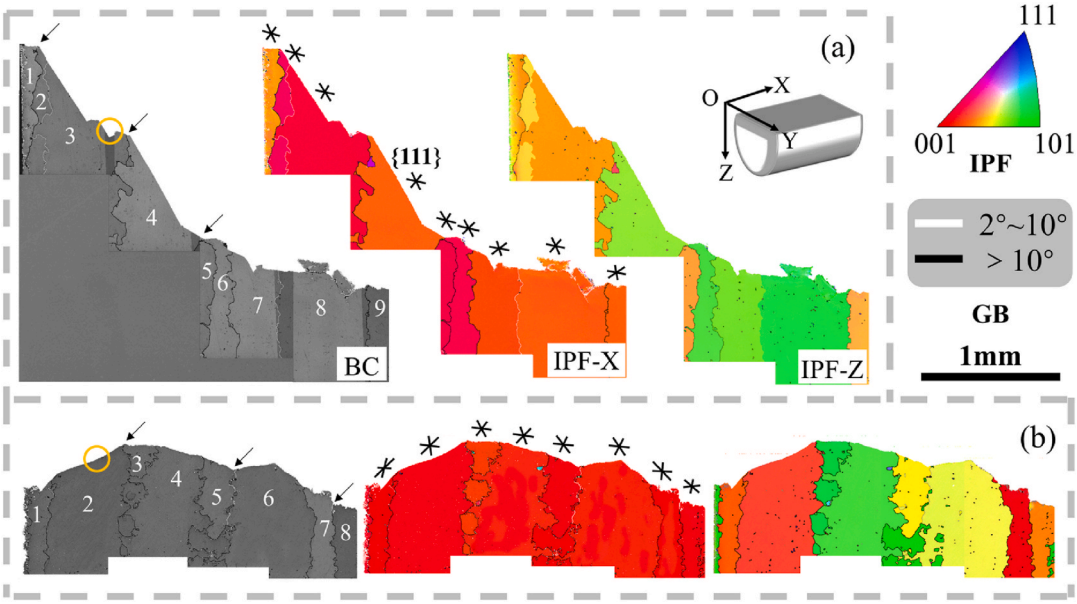

Fig. 6. DZ125 crack path deflection analysis via the EBSD performed on the cross-section of the fracture surface: (a) mechanical polishing, $\sigma_a = 300$ MPa and 850 °C, $N_f = 6.87 \times 10^7$; (b) electrolytic polishing, $\sigma_a = 250$ MPa and 1000 °C, $N_f = 4.91 \times 10^6$. Note: black arrows indicate the considerable change in crack path. The {111} slip plane traces are indicated in the IPF-X to aid interpretation. XY plane indicates the longitudinal cross-section, X-direction is parallel to the fatigue load axis, and Z-direction is normal to the cross-sectional plane.

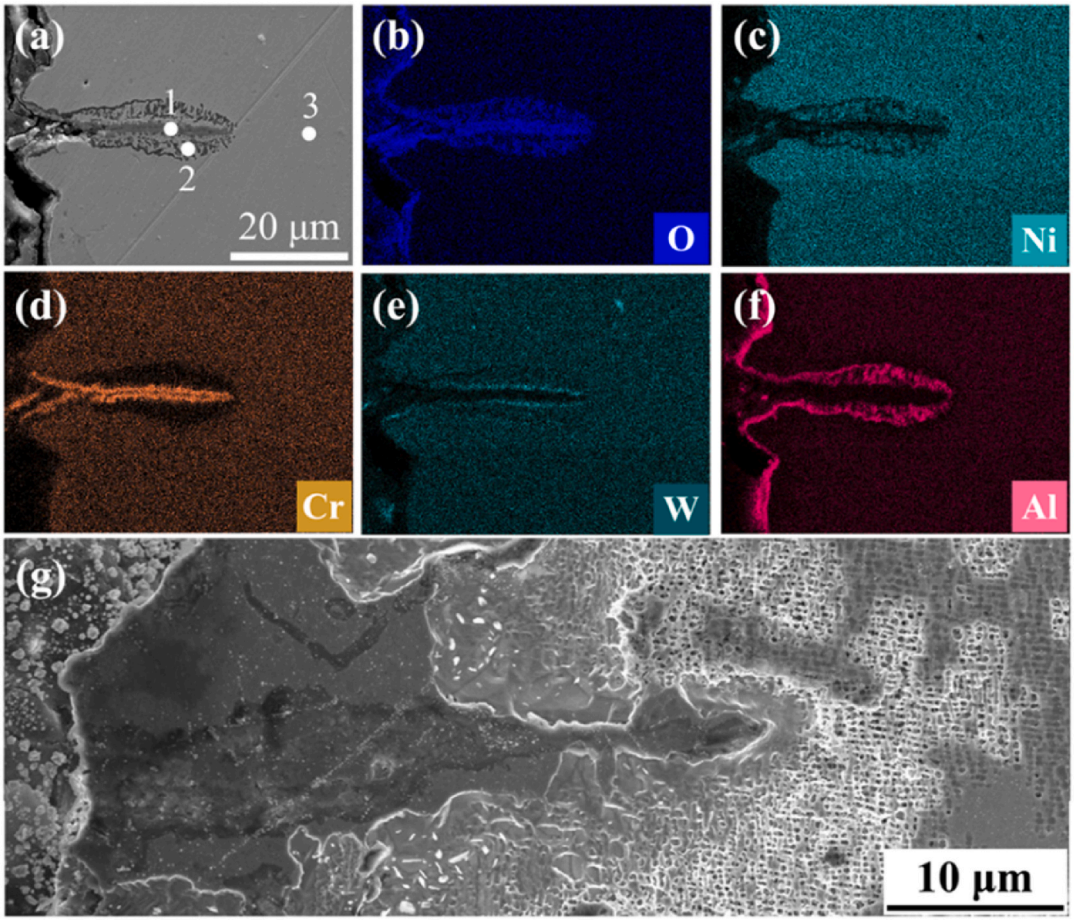

Fig. 7. SEM micrograph in (a) and corresponding EDS mapping in (b) to (f), performed on the cross-section of the DZ125 specimen, prepared down to electrolytic polishing, tested at $\sigma_a = 225$ MPa and 1000 °C, with a fatigue life of $N_f = 9.68 \times 10^7$; (g) SEM micrograph taken from the etched sample. The numbers in (a) indicate the EDS measurement positions in Table 2.

was measured to be 35.2 ± 14.2 μm in average, with the maximum length of 60.2 μm and minimum length of 9.6 μm.

Fig. 5d and e shows the SEM cross-sectional view of the DD6 alloy. At 1000 °C, the fatigue fracture was characterised by the Stage I cracking, Fig. 5d, although the enlarged view did reveal an internal oxide penetration and associated fatigue cracking. The average crack length was 77.9 ± 18.5 μm with the maximum length of 96.2 μm and minimum length of 59.2 μm. At 1100 °C, the cross-sectional view in Fig. 5e confirms the nature of Mode I cracking. The enlarged view of the region highlighted by blue in Fig. 5e indicates an oxidised region subjacent the fracture surface, while that highlighted by red in Fig. 5e reveals an oxide penetration induced fatigue crack having a length of 104.0 μm. The average crack length for the 1100 °C DD6 specimen was measured to be 68.2 ± 30.5 μm.

The distinctive fracture mode difference between the two considered superalloys is the presence of mixed Stage I and Mode I in the columnar-grained DZ125 while either pure Stage I or Mode I in the single-crystal DD6 (Fig. 5). The columnar grain boundaries parallel to the fatigue loading axis might play a certain role. To test the hypothesis, a series of EBSD scans were performed on the cross-section of the fracture surface to identify the grain orientations, from which the slip traces of {111} planes can be derived along the crack path. Details about the EBSD data processing and their interpretations including the inverse pole figure (IPF), kernel average misorientation (KAM) and band contrast (BC) maps can be found in Refs. [22–24].

Fig. 6a presents the BC, IPF-X and IPF-Z maps collected from the 850 °C, while those from the 1000 °C DZ125 specimen is shown in Fig. 6b; both specimens exhibited the Stage I followed by Mode I fracture characteristics. The high-angle grain boundaries (HAGBs, defined by the misorientation angle of >10°) and the low-angle grain boundaries (LAGBs, between 2 and 10°) are indicated with the black and white, respectively. In general, the crack path deflection is induced by HAGBs because the crack is following {111} slip traces in each grain. In other words, the high misorientation angle between adjacent grains could cause the crack path deflection. For example, the misorientation angle between grains 1 and 2 in Fig. 6a were measured as 42.3°, and 41.7° for grains 3 and 4. As a result, the crack path turned away from the horizontal plane in the former, while a hump existed in the latter. As a comparison, there was very little crack path change in the region between grains 2 and 3 separated by an LAGB, Fig. 6a. When the crack length becomes sufficiently large (comparable to a couple of grains), the far-field stress seems to play a predominant role, resulting in the shift from the crystallographic Stage I to Mode I propagation (beginning from grain 7 in Fig. 6a while grain 8 in Fig. 6b).

3.4. Oxidation, recrystallisation and strain localisation

A representative oxide penetration found in DZ125, tested at σ_a = 225 MPa and 1000 °C with a fatigue life of $N_f = 9.68 \times 10^7$, is shown in Fig. 7a, and the corresponding EDS maps of O, Ni, Cr, W and Al elements, are presented in Fig. 7b–f, respectively. Two distinct oxide layers existed, with the outer layer being Cr-enriched (Fig. 7d) while the inner layer being Al-rich (Fig. 7f). In-between, there was a thin but measurable W-rich oxide layer (Fig. 7e). Furthermore, Fig. 7g provides evidence of γ′ to γ phase transformation, induced by Al atoms diffusion to form Al-rich oxides. This resulted in the formation of γ′-depleted areas and modified

Table 2
Summary of EDS determined compositions of oxides in DZ125 (all in wt.%).

Positions in Fig. 7a	O	Ni	Cr	W	Al	Ti	Hf	Mo	Ta	Co	C
1	24.5	12.1	43.7	2.8	0.8	1.9	1.5	N/A	2.4	4.1	6.2
2	8.2	47.7	1.7	12.8	9.2	0.3	4.3	2.8	1.5	8.0	3.5
3	0.5	59.7	4.1	11.9	4.2	0.9	3.6	0.7	2.8	8.2	3.4

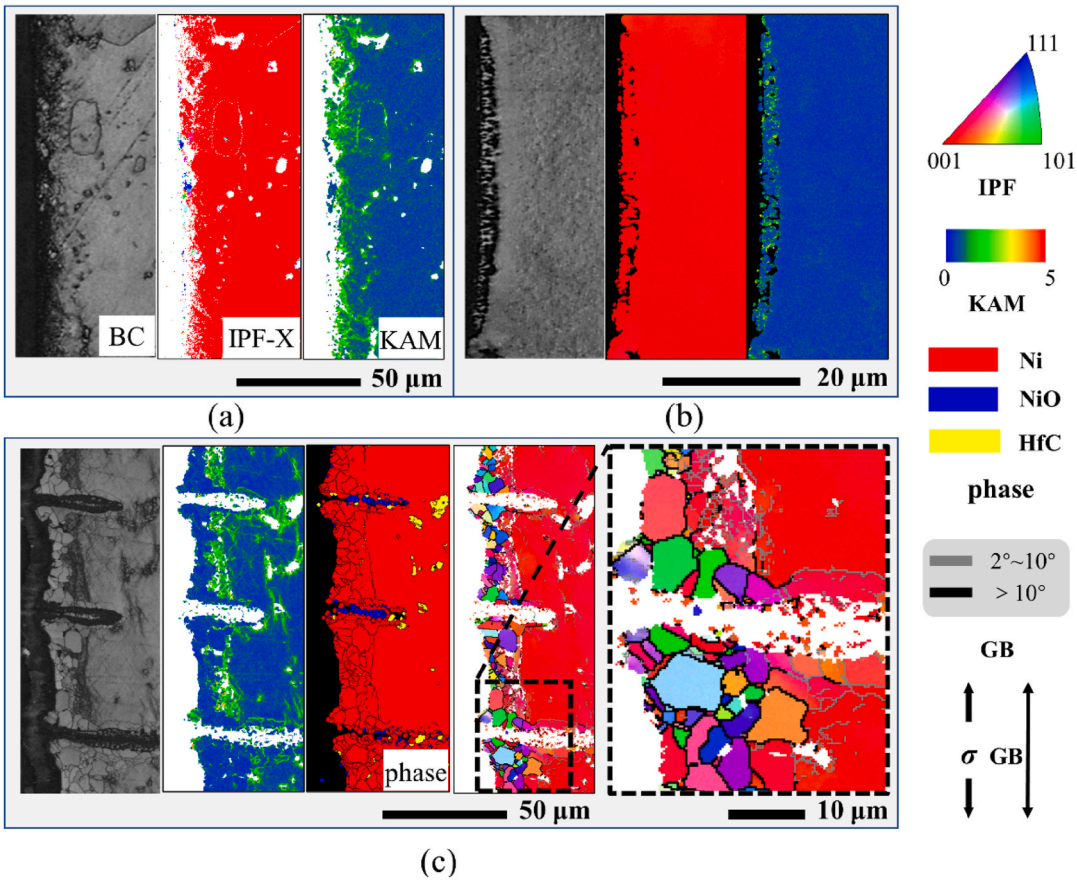

Fig. 8. EBSD analysis of the surface recrystallisation and oxidation in DZ125 specimens: (a) mechanical polishing, $\sigma_a = 300$ MPa and 850 °C, $N_f = 6.87 \times 10^7$; (b) electrolytic polishing, $\sigma_a = 250$ MPa and 1000 °C, $N_f = 4.91 \times 10^6$; (c) mechanical polishing, $\sigma_a = 225$ MPa and 1000 °C, $N_f = 9.68 \times 10^7$. Based on the SEM fractography, the specimens in (a) and (b) are characterised by the Stage I followed by Mode I, while that in (c) is characterised by Mode I. Note: the annotation of KAM and phase stand for the kernel average misorientation and phase maps, respectively.

γ/γ′-microstructure below the oxidised layers (adjacent to the crack face, ahead of the crack tip and near-surface regions), Fig. 6g. The EDS point analysis is given in Table 2 for the outer and inner oxides with reference to the metal matrix, confirming that the oxides in DZ125 were primarily composed of Al_2O_3 and Cr_2O_3. In the work on DD6 at 1000 and 1100 °C [3], the internal oxide penetration was found to consist of Al_2O_3 and Cr_2O_3.

Fig. 8 presents the characteristics of surface recrystallisation and oxidation in DZ125, as revealed by the EBSD analysis performed on the cross-section. EBSD maps presented in Fig. 8a and b are solely for the nickel matrix, and thus the non-indexed regions would be either oxides or carbides depending on their locations. In addition, the phase map in Fig. 8c highlights the Hf-rich MC type carbides in yellow and NiO in blue. Oxides often come with mis-indexing due to their severe charging problems, causing poor Kikuchi pattern quality. Thus, the blue NiO in the phase map of Fig. 8c only serves as an indication of oxide location.

For the 850 °C post-fatigued specimen (6.87×10^7 cycles) with a surface finish of mechanical polishing, local strain concentration appeared in the surface region, extending to the subsurface with a depth of 15 μm, see the KAM map in Fig. 8a. Furthermore, neither the oxide penetration nor crack was found, although some uniform oxidation might have already formed at 850 °C. For the 1000 °C specimen that had received an electrolytic polishing, the formation of inner oxide layer consisting of alternating nickel matrix and oxidised material (Al_2O_3, according to Refs. [25,26]) can be seen in Fig. 8b. Again, the strain localisation appeared near the surface, but there was no sign of recrystallisation or internal oxide penetration.

As a comparison, for the mechanically polished DZ125 specimen tested at 1000 °C with a fatigue life of 9.68×10^7, the IPF and band contrast maps in Fig. 8c show evidently the surface recrystallisation up to a depth of 15 μm. The KAM map confirms the very low intragranular misorientation in the recrystallised grains. In their subjacent region, both the band contrast and KAM maps indicate the localised plastic deformation extending up to a couple of microns in depth. Furthermore, the enlarged view of the IPF map in Fig. 8c, taken from a typical oxide penetration, reveals the presence of LAGBs in the crack flanks and the subsurface of the recrystallised grains. These regions seem to be prone to recrystallisation at later stage. The highly deformed region is also visible in the vicinity of the penetrated oxide and crack tip. A small number of patchy grains with different orientations can be seen in the IPF map of

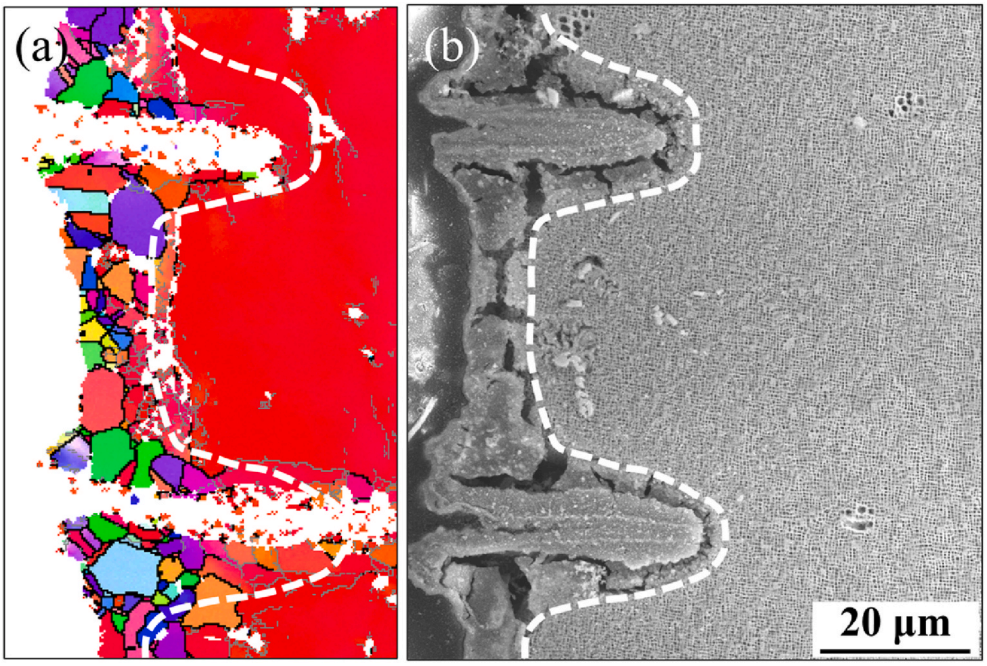

Fig. 9. Comparison between recrystallisation region and γ′ depleted region as observed in DZ125 tested at $\sigma_a = 225$ MPa and 1000 °C, $N_f = 9.68 \times 10^7$: (a) EBSD IPF-X, the same one shown in Fig. 8c; (b) etched specimen using a solution containing 5 g $CuSO_4$, 15 mL HCl and 25 mL H_2O to preferentially dissolve the γ′-precipitate, thereby leaving the γ-phase in the micrograph. Note: the dashed line indicates the boundary of γ′ depleted region.

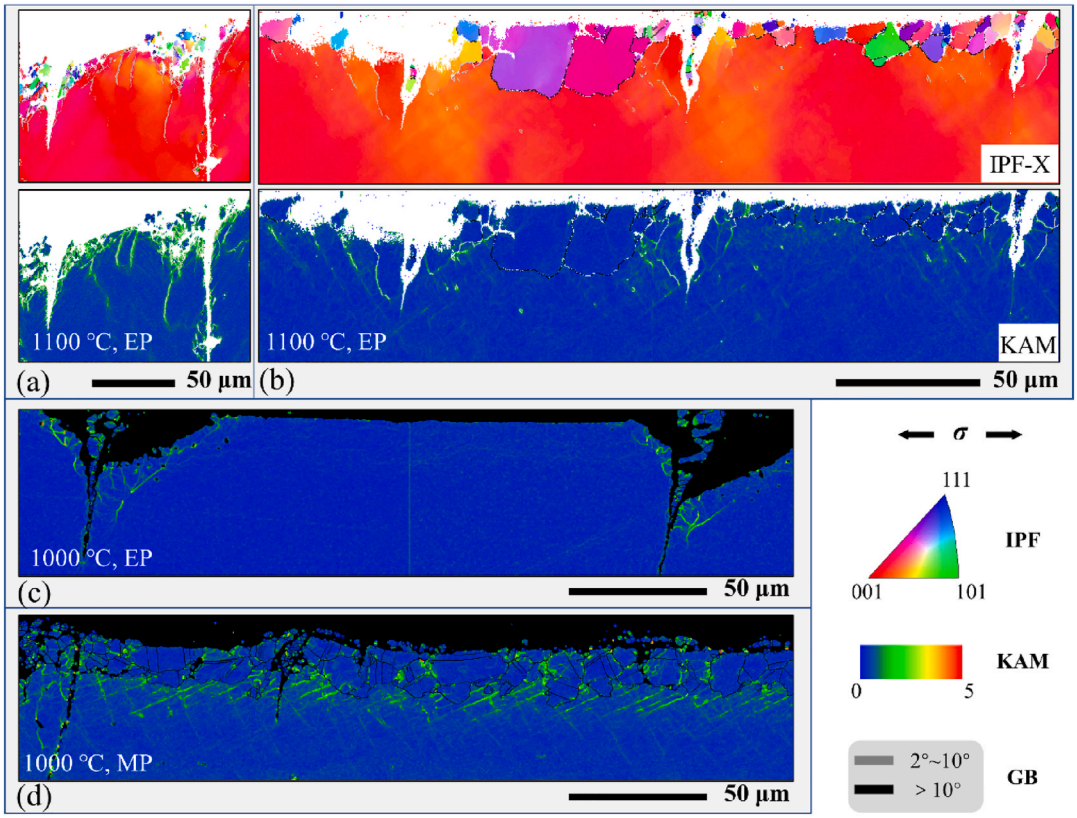

Fig. 10. EBSD analysis of the surface recrystallisation and oxidation in DD6 specimens: (a) electrolytic polishing, $\sigma_a = 200$ MPa and 1100 °C, $N_f = 8.63 \times 10^7$; (b) electrolytic polishing, $\sigma_a = 200$ MPa and 1100 °C, $N_f = 1.51 \times 10^8$; (c) electrolytic polishing, $\sigma_a = 175$ MPa and 1000 °C, $N_f = 7.77 \times 10^8$; (d) mechanical polishing, $\sigma_a = 175$ MPa and 1000 °C, $N_f = 1.62 \times 10^9$. Specimens in (a) and (b) are characterised by Mode I, while that in (c) and (d) are characterised by Stage I cracking. Note: electrolytic polishing and mechanical polishing are abbreviated as EP and MP, respectively.

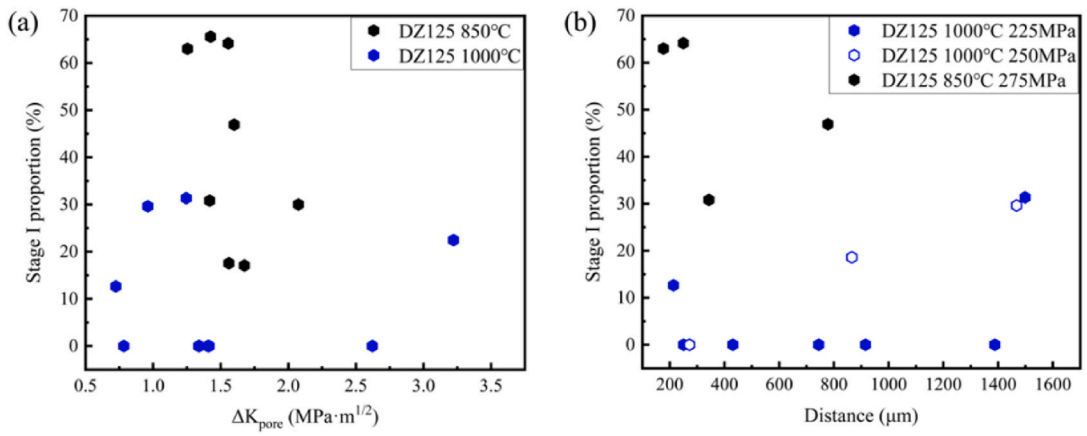

Fig. 11. Relationship between the Stage-I area proportion and two casting pore characteristics in DZ125 alloy: (a) calculated stress intensity factor amplitude around the pore, ΔK_{pore}; (b) distance of the pore to the specimen surface.

Fig. 8a. Their presence might suggest recrystallisation [27], but they can also be attributed to material fragmentation due to fracture or metallographic sample preparation. Given their infrequency and very small size, especially when compared to Fig. 8c, it is judged that there was no recrystallisation in Fig. 8a. Note that the surface recrystallisation observed in Fig. 8c seems to be correlated with the γ′ depleted region, as evidenced by the etched sample condition, Fig. 9. This phenomenon can be interpreted that the formation of γ′ depletion increases the susceptibility of material recrystallisation, by providing recrystallisation nuclei [28] and reducing grain growth barrier [28,29].

For the single-crystal DD6 specimen (electrolytic polishing) after 8.63×10^7 fatigue cycles at 1100 °C, two representative internal oxide penetrations are illustrated in Fig. 10a. First, there was no recrystallisation at the surface region between the two oxides in the IPF map. The seemingly recrystallised grains close to the oxide root were likely owing to the material fragmentation due to fracture. This postulation is supported by the KAM map in Fig. 10a, where these small grains contained high intragranular misorientation. Second, at the blunted oxidation crack tip, newly developed small fatigue cracks appeared and propagated in the matrix. The highly localised deformation developed at the crack tip and flanks. Fig. 10b presents the recrystallisation and oxidation associated cracks found in another 1100 °C specimen (electrolytic polishing). In this case, the surface recrystallised grains can be seen clearly in the regions between the two penetrated oxides (IPF map). The localised high plastic deformation in the vicinity of fatigue crack tip can extend up to 20 μm in depth (KAM map).

Figs. 10c and d shows the KAM maps obtained from the 1000 °C specimens. The presence of surface recrystallisation can be evidenced by the KAM map overlapped with the HAGBs in the specimen that had received mechanical polishing, Fig. 10d. As a comparison, for the specimen that had received electrolytic polishing, the KAM map in Fig. 10c shows the absence of HAGB in the regions between the two penetrated oxides. Collectively, these results suggest that internal oxidation can trigger the fatigue crack initiation. Whether the recrystallisation occurs or not does not necessarily alter the propensity of oxidation induced Mode I cracking.

4. Discussion

4.1. Factors influencing the crack initiation and propagation behaviour

The distinctive fracture-mode discrepancy between the columnar-grained DZ125 and single-crystal DD6 lies in the presence of Stage I cracking followed by Mode I propagation in DZ125 (Fig. 2 and comparing Fig. 3a and d with Fig. 4a). The DZ125 specimens exhibiting such crack characteristics present different Mode-I proportions over the fracture surface (Table S2). In Section 3.3, referring to Fig. 6, one plausible explanation has been given in terms of the diminishing role of microstructure-related factor (i.e. grain orientation and related {111} slip planes) when the crack length is considerably large. Since the crystallographic Stage I region consists of both the crack initiation and early-stage propagation [10], the location and size of the casting pore, which has been observed as the crack initiator especially in the VHCF regime (e.g. Refs. [4,5,10,13,30]), deserves our attention.

To this end, these two casting-pore related parameters were quantitatively measured and summarised in Table S2. Note all the size measurements made on the fracture surface were based on the projected area (the load axis of fatigued samples was parallel to the beam in the SEM chamber). As a result, stress intensity factor amplitude around the pore, ΔK_{pore}, can be worked out through the equation proposed by Murakami et al. [31] with the shape factor of 0.5.

$$\Delta K_{pore} = 0.5\sigma_a\sqrt{\pi\sqrt{A_{pore}}} \quad (1)$$

where A_{pore} is the surface area of the pore and σ_a is the stress amplitude. Fig. 11a presents the calculated ΔK_{pore} versus the Stage I proportion for DZ125 at 850 and 1000 °C, revealing neither a positive nor negative correlation. Also, the Stage I proportion does not depend on the pore distance to surface, Fig. 11b. These observations indicate that the pore size or its location is not a controlling factor for the shift from Stage I to Mode I crack path.

Although the Stage I to Mode I crack path transition as observed in the columnar-grained DZ125 can be attributed to the crack length increase, which changes the controlling factor from microstructure to far-field stress, the role of grain boundaries parallel to the fatigue load axis should not be neglected. Compared to the single-crystal DD6 (i.e. absence of the HAGB), that is characterised by a pure Stage I cracking 1000 °C (Figs. 4b and 5d), it is reasonable to conclude that the HAGBs in DZ125 can also cause the crack path deflection, potentially affecting the Stage-I proportion. Strictly speaking, the observed influence of HAGBs on crack propagation mode transition is only applicable to the considered temperature range from 850 to 1000 °C, because of the temperature-dependent crystal plasticity [32].

In the presence of internal oxide penetration at high temperatures, the tendency to form Mode I fracture surface is increased (Figs. 3 and 4, and Table S2). The SEM identified internal oxides at the subjacent region (Fig. 5c and e) provide evidence in addition to the parallel cracks initiated from the oxide intrusion (Figs. 8c and 10). For many Ni-base superalloys (e.g. René series N5, N4, N500 and N515, CMSX-4, AM1 and TMS-238) containing blocky MC carbides with the alloy concentrations of Ta, Nb, Hf and W, it is known that the carbides oxidise faster than the γ/γ′ matrix [33–35]. The selective carbide oxidation would

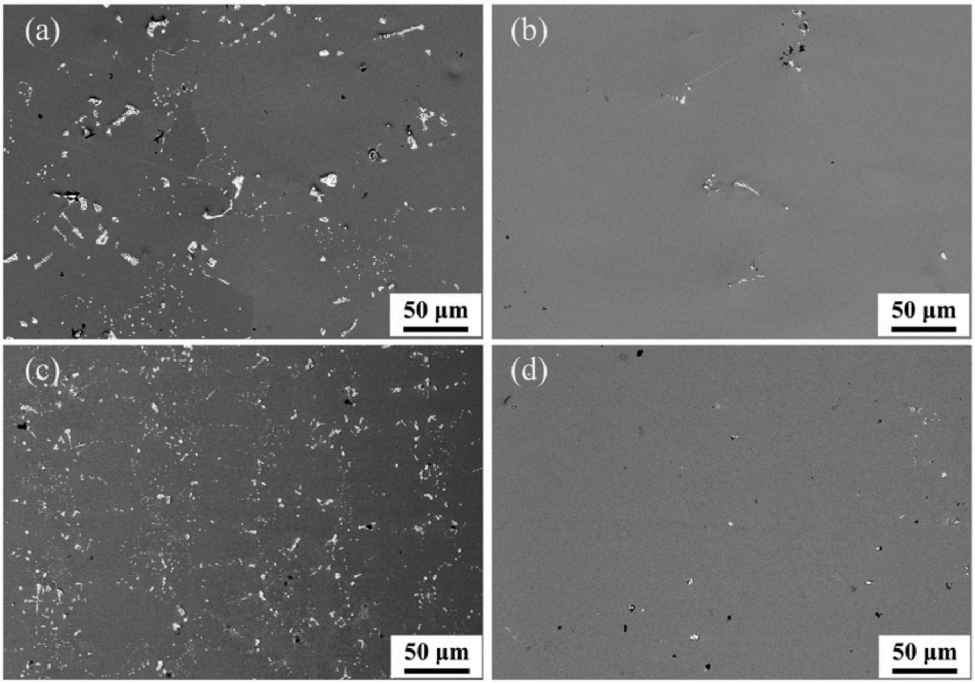

Fig. 12. Backscattered electron SEM micrographs showing the surface carbide distribution: (a) DZ125 in pre-test condition; (b) DD6 in pre-test condition; (c) DZ125 in 20 min thermally exposed condition at 1000 °C; and (d) DD6 in 20 min thermally exposed condition at 1100 °C. Note: vertical direction is along the fatigue axis, which is also parallel to the grain boundaries for DZ125. All specimens had the electrolytically polished surface finish.

cause volume expansion and act as a stress raiser to promote crack initiation [36–39]. However, in the present work we observe no selective oxidation associated with carbides for both the DZ125 and DD6, despite their presence in the material (Figs. S1 and S2).

To further validate the above-mentioned finding, additional SEM observations of the surface carbide morphology and distribution were performed on electrolytically polished DZ125 and DD6 specimens by comparing their before and after thermal exposure (1000 °C for 20 min) conditions. Results are summarised in Fig. 12. For the DZ125, the large-sized blocky carbides become smaller due to carbide decomposition (comparing Fig. 12a with 12c). This probably explains why the selective carbide oxidation does not contribute to the oxide penetration. Also, the fatigue loading axis is parallel to the directional solidification (i.e. columnar grain boundaries, HAGBs). The oxygen diffusion rate is known to be positively correlated to the angle between the loading axis and the HAGB [38,39], indicating that the present loading scenario does not favour the selective carbide oxidation [16,40,41]. For the DD6, the low C content (Table 1) significantly reduces the carbide number density in both the prior to and post thermal exposure conditions, Fig. 12b and d. Therefore, the internal oxide penetration (Figs. 7, 8c and 10) should not be misinterpreted with the preferential dendrite (or grain) boundary oxidation as reported in previous work [39,42–44]. Note that the selective carbide oxidation and its consequence on high-temperature fatigue behaviour are worthwhile to be explored further. This is because the present conclusion might only apply to the two specific superalloys and VHCF conditions considered.

Although SEM cross-sectional observation (e.g. Fig. 5c and e) shows the clear correlation between internal oxide penetration and Mode I fracture, the twofold nature of oxidation: crack closure effect vs. oxide embrittlement [45], means that the presence of surface oxides does not always lead to the Mode I fracture. One question arises as to whether the observed Mode I cracking is solely attributed to the oxidation, or the combined effect of oxidation and recrystallisation? This is particularly intriguing as the recrystallisation was also found in the specimen surface (Figs. 8c, 10b and 10d). Indeed, both processes occur at the material surface and depend on the interplay of time, stress and temperature. If the observation made on the fractured specimens does not provide unambiguous evidence about at what stage the recrystallisation is formed (e.g. before or after the oxide penetration, crack initiation, or specimen fracture), then it is only possible to limit one process while bringing out the other. Therefore, interrupted VHCF tests were performed at 1000 °C and 225 MPa for the DZ125 (1.00×10^7 cycles) while 1100 °C at 200 MPa for the DD6 (1.35×10^7 cycles). Both specimens had received an electrolytic polishing prior to the VHCF test and the post-mortem EBSD analysis confirms no surface recrystallisation (Fig. 13a and c). But the internal oxide penetration can still be observed in both specimens, corroborating that the surface grain recrystallisation is not a prerequisite for the oxide penetration, neither for the Mode I cracking.

The EDS elemental mapping performed on the two interrupted fatigue specimens reveals the oxide nature – Al_2O_3 and Cr_2O_3 as the primary constituents with W-rich layer in-between (Fig. 13b and d). This observation is consistent with the result obtained from the fractured specimens (Fig. 7). There are two key coupled mechanisms that contribute to crack initiation in Ni-base superalloys: oxide penetration and oxide spallation [25]. Adhesive oxide scales, like those deposited on uncoated Ni-base superalloys [46,47], are prone to surface roughening and corroding with fatigue. Cross-section of the interrupted DZ125 specimen (1.00×10^7 cycles, Fig. 13b) shows an incipient oxide intrusion with the outer oxide still attached to the specimen surface. With continued fatigue loading, the mismatch in elastic modulus at the oxide and metal interface leads to localised stresses (KAM maps in Figs. 8 and 10) that can exceed the critical fracture strength of the oxide. The oxide fracture exposes the fresh part of substrate surface, promoting the formation of channels of damage that penetrate into the subsurface [48]. The repetition of this mechanism tends to localise oxidation, developing a critical zone where a fatigue crack can initiate easily. In other words, fatal-crack initiation in DZ125 and DD6 at high-temperature VHCF can result from interactions between oxidation and fatigue. Eventually, fatigue-dominant microcrack growth overtakes the oxidation and rupture mechanism. Our oxidation-fatigue interaction observation also implies that the oxide embrittlement seems to be predominant under VHCF loading, when compared to the crack closure or plastic blunting

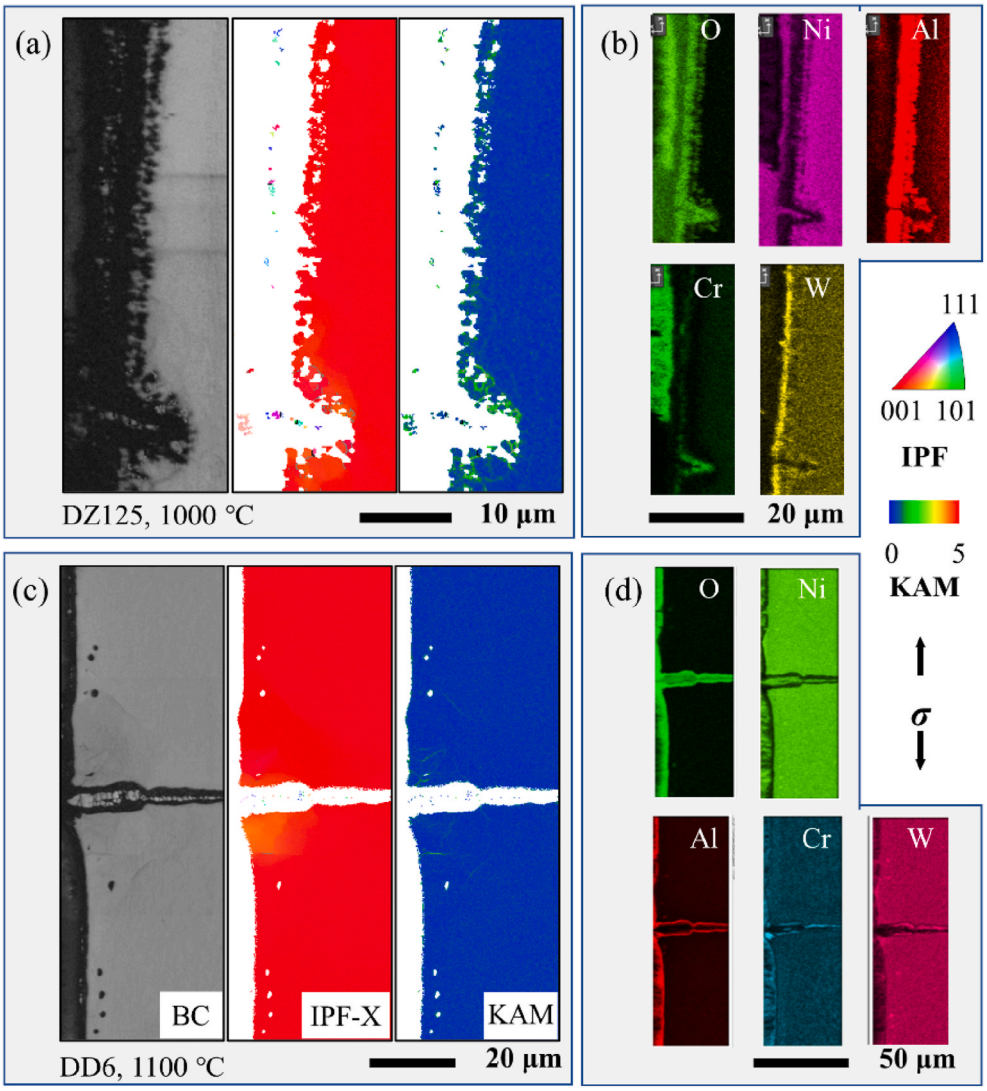

Fig. 13. Interrupted VHCF specimens: (a) and (b) DZ125, electrolytic polishing, $\sigma_a = 200$ MPa and 1000 °C, test interrupted at 1.00×10^7 fatigue cycles; (c) and (d) DD6, electrolytic polishing, $\sigma_a = 200$ MPa and 1100 °C, test interrupted at 1.35×10^7 fatigue cycles. (a) and (c) EBSD observation revealing no recrystallisation while (b) and (d) EDS analysis confirming the oxide nature.

Table 3
Summary of VHCF specimens selected for the EBSD analysis. For comparison purposes, EBSD results from the previous work [3] on DD6 at 1000 °C are included. RX: recrystallisation.

Alloy	Surface finish	Stress (MPa)	Temp. (°C)	Fatigue cycles	Fracture characteristics	Key observations
DZ125	Mechanical polishing	300	850	6.87×10^7	Stage I followed by mode I	No RX, uniform oxidation, no penetration and no crack
		225	1000	9.68×10^7	Mode I	RX, uniform oxidation, penetration and cracks
	Electrolytic polishing	250	1000	4.91×10^6	Stage I followed by mode I	No RX, uniform oxidation, no penetration and no crack
		225	1000	1.00×10^7	Interrupted test	No RX, uniform oxidation, penetration and cracks
DD6	Electrolytic polishing	200	1100	1.51×10^8	Mode I	RX, uniform oxidation, penetration and cracks
		200	1100	8.63×10^7	Mode I	No RX, uniform oxidation, penetration and cracks
		200	1100	1.35×10^7	Interrupted test	No RX, uniform oxidation, penetration and cracks
DD6 [3]	Mechanical polishing	175	1000	1.62×10^9	Stage I	RX, uniform oxidation, penetration and cracks
	Electrolytic polishing	175	1000	7.77×10^8	Stage I	No RX, uniform oxidation, penetration and cracks

process.

After elucidating the predominant role of oxidation on Mode I cracking, let's shift our focus to the surface recrystallisation. To facilitate the discussion, all the key EBSD and EDS observations are summarised in Table 3. The comparison of the electrolytically polished vs. mechanically polished specimens leads us to conclude that the surface grain recrystallisation can occur under both surface finish conditions. By contrast, test duration and temperature seem to play more important role in controlling the surface recrystallisation of the DZ125 and DD6 superalloys.

4.2. Fatigue life and its prediction

A question arises as to whether stage I followed by mode I propagation behaviour in DZ125 would lead to any measurable fatigue-life difference when compared to the DD6. Previous work by Cervellon

et al. [4] revealed no noticeable difference in the VHCF fatigue life between all investigated superalloys (six different grades) under fully reversed conditions ($R = -1$). Our recent work on DD6 also reached a similar conclusion by comparison with the CMSX-4 and its plus version [3]. Therefore, a comparative study can be performed by grouping the data points concerned, namely, those exhibiting Stage I followed by Mode I (DZ125) and the pure Stage I (DD6) in Fig. 2. The Basquin equation $\sigma_a = \sigma_f'(2N_f)^b$ was used to obtain the S–N curve fitting (Fig. S3), where σ_f' is the fatigue strength coefficient and b is the fatigue strength exponent. The DD6 and DZ125 superalloys exhibit a similar fatigue-life dependency on stress amplitude, despite their distinct crack propagation path. This might be understood by the fact that crack-initiation stage accounts for more than 90% of the life, especially for the high-cycle fatigue and VHCF [49–53].

Microstructure characterisation is not the goal in itself. The capability to establish the VHCF fatigue life prediction model based on the characterised casting-pore characteristics (Table S2) is deemed to be important to prevent the pre-mature fatigue failure of safety-critical parts/components. Our SEM fractographies reveal three types of cracking characterised by the Stage I followed by Mode I (850 °C DZ125), pure Stage I (1000 °C DD6), and Mode I (1000 °C DZ125), respectively. Note that the 1100 °C DD6 VHCF dataset is not included here as no visible pore on the fracture surface. Moreover, the Stage I followed by Mode I can be grouped with the pure Stage I, given that the crack initiation consumes more than 90% of the total fatigue life [10,54,55]. We thereby only need to consider two primary cracking scenarios: the Stage I crack initiation and early-stage growth driven by a mixed Mode I and Mode II loading (abbreviated as K_{OCT} for describing the driving force for propagating a crack along the slip plane) [56], and its simplified version driven by Mode I loading (abbreviated as K_I for describing the driving force for propagating a crack under a pure tensile stress normal to the crack plane).

For the K_{OCT} calculation, Telesman and Ghosn [57] combined the Mode II stress intensity factor (K_{RSS}) that drives dislocation slip and the resolved stress acting normal to the slip plane (K_{RNS}) that contributes to the crack opening by:

$$K_{OCT} = \sqrt{K_{RSS}^2 + K_{RNS}^2} \tag{2}$$

For a perfectly grown crystal along the [001]-direction, the angle between the fatigue load axis and slip plane normal (φ), and the angle between the load axis and slip direction (θ), for the {111}<1 $\bar{1}$ 0> slip system can be worked out as 54.7° and 45.0°, respectively. Therefore, the relationship of K_{RSS} and K_{RNS} with the K_I is found:

$$\begin{aligned} K_{RNS} &= K\cos^2\varphi \\ K_{RSS} &= K\cos\theta\cos\varphi \end{aligned} \tag{3}$$

Substituting Eq. (3) into Eq. (2) leads to the relationship of $K_{OCT} = 0.527K_I$.

Note that the magnitude of ΔK_{pore} (calculated by Eq. (1) providing the value range from 0.57 to 3.22 MPa $m^{1/2}$, Table S2) are much lower than the typical value of ΔK_{th} for propagating a long fatigue crack (e.g. ~10 MPa $m^{1/2}$ for AM1 superalloy at 950 °C [58]). Fatemi et al. [59] developed a fatigue indicator parameter (FIP) method based on the critical plane approach that can describe small fatigue crack initiation and growth in single-crystal copper [60] and cast iron [61]. This FIP method has been adapted by Steuer et al. [13] to capture the crack initiation size dependence as observed in low-cycle fatigue of AM1 at 750 °C, with the equation given below:

$$\text{FIP} = \frac{\mu\Delta\sigma}{E}\left(1 + k\frac{\Delta K_{pore}}{\Delta K_{th}}\right) \tag{4}$$

where μ is the Schmid factor ($\mu = \cos\theta\cos\varphi$ referring to Eq. (3)) for octahedral slip with a value of 0.408 for a perfectly [001] aligned alloy bar by assuming no difference between the exact orientation of fatigue specimens and the alloy bar. $\Delta\sigma$ is the applied positive stress range, which is same as the σ_a under $R = -1$. E is the Young's modulus (96 GPa for 850 °C, 84 GPa for 1000 °C DZ125, and 78 GPa for 1000 °C DD6 [62]) and parameter k is a constant taken as 1 [13]. ΔK_{th} in Eq. (4) is an intrinsic material parameter affected by temperature. In accordance with the literature, $\Delta K_{th} = 1.18$ MPa $m^{1/2}$ was used for DZ125 850 °C [10] while $\Delta K_{th} = 10$ MPa $m^{1/2}$ for DZ125 1000 °C and DD6 1000 °C [63]. The calculated FIP-values can then be used to obtain the curve fitting against the experimentally determined cycles to failure. Thereafter, a one-to-one plot comparison can be made in terms of predicted vs. experimentally determined fatigue lives.

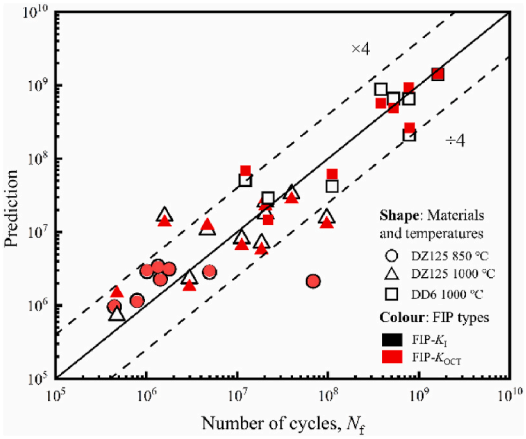

Fig. 14. Comparison of the model prediction with experimentally obtained fatigue lives. Note: For the predicted fatigue lives, $\Delta K_{th} = 1.18$ MPa $m^{1/2}$ was used for DZ125 850 °C while $\Delta K_{th} = 10$ MPa $m^{1/2}$ for DZ125 1000 °C and DD6 1000 °C.

Table 4
Comparison of FIP-values by accounting for the [001]-direction misalignment while using the K_{OCT} (DD6, 1000 °C).

Stress	Fatigue life	FIP-K_I ($\times 10^{-3}$)	FIP-K_{OCT} ($\times 10^{-3}$)	Misalignment angle	Corrected FIP-K_{OCT} ($\times 10^{-3}$)
250	2.19 × 10^7	1.44	1.44	4.8	1.42
225	1.11 × 10^8	1.37	1.28	6.3	1.25
200	3.82 × 10^8	1.11	1.08	6.3	1.05
200	5.24 × 10^8	1.12	1.09	4	1.08
200	7.86 × 10^8	1.20	1.13	4	1.12
175	7.77 × 10^8	1.09	1.01	4	1.00
175	1.62 × 10^8	1.04	0.98	4.8	0.97

Comparison of the predicted fatigue lives and experimentally obtained ones for both the DZ125 and DD6 are shown in Fig. 14. The model predictions are within a factor of four of the experimental results, which is not as good as the previous work (a factor of two in Ref. [63] while a factor of three in Ref. [10]). Interestingly, little difference exists between the K_{OCT} and K_I based fatigue-life predictions. This can be understood from the FIP vs. N_f plot (Figs. S4a–S4c), where using the K_{OCT} fails to reduce the data scatter. Also, an outlier ($N_f = 6.87 \times 10^7$) in the DZ125 data plot of Fig. 14 can be seen. According to the SEM fractography (Fig. S4d), this specimen contains a couple of casting pores within the fatal-crack initiation region, which is atypical one.

It was noted in Ref. [13] that the exact orientation of the tested single-crystal specimen could cause the fatigue data scatter. The misalignment with respect to the [001]-direction would lead to a

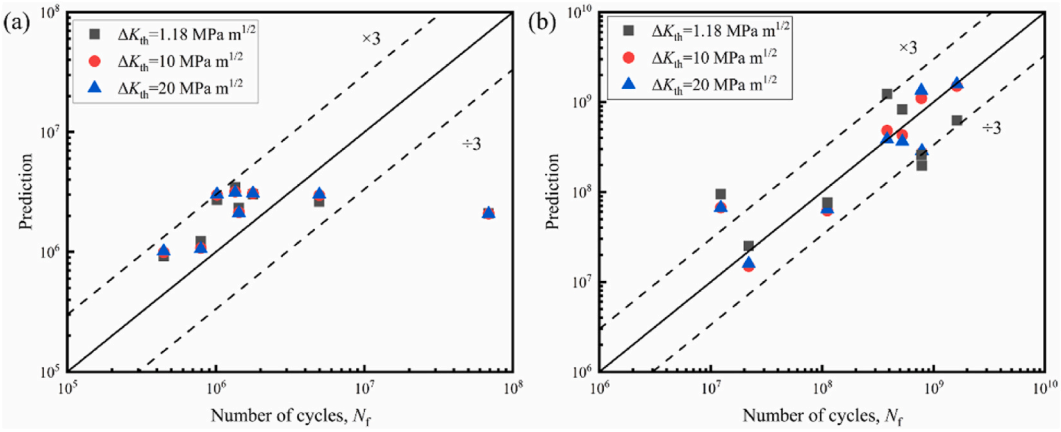

Fig. 15. Model predicted fatigue lives in comparison with the experimental data using different threshold values of the stress intensity factor amplitude: (a) 850 °C DZ125; (b) 1000 °C DD6.

different K_{OCT}, referring to Eqs. (2) and (3). Also, such misalignment would affect the values of Schmid factor μ as well as the Young's modulus E in the FIP approach in Eq. (4). Table 4 shows the measured misorientation angle of selected DD6 specimens. Surprisingly, the effect of [001]-direction misalignment on the fatigue life prediction is insignificant (Fig. S5). The calculated difference is within 2.42% when compared to that under the assumption of a perfect alignment.

To the best of the authors' knowledge, the value selection of ΔK_{th} was either based on the long crack propagation threshold value (10 MPa m$^{1/2}$ for a group of superalloys) [63] or data extrapolation of the ΔK_{pore} vs. N_f curve to obtain the minimum value (1.18 MPa m$^{1/2}$ for DZ125) [10]. Development from small fatigue cracks to a long major crack is known to be affected by many factors (material type and microstructure, loading mode, environment, etc.) [64]. It is certainly beyond the scope of the present work to determine the accurate value of ΔK_{th} for Ni-base superalloys. However, a review paper by Hong et al. [65] has summarised the ΔK_{th} value ranges for steels, aluminium, titanium and magnesium alloys to be 4.0 to 6.0, 1.5 to 2.8, 3.4 to 4.0 and 1.3–1.5 MPa m$^{1/2}$, respectively. This stimulates us to perform a sensitivity study by assessing the impact of the chosen ΔK_{th}-value (three values of 1.18, 10 and 20 MPa m$^{1/2}$) on the model prediction accuracy. We observe little dependence of the predicted fatigue lives on the ΔK_{th}-value, Fig. 15. Further research is needed to study the underlying reason.

5. Conclusions

Based on the quantitative fractography combined with cross-sectional observation performed on the columnar-grained DZ125 and single-crystal DD6, subjected to high-temperature very-high-cycle fatigue loading, the following conclusions can be made:

1) In the absence of oxidation, the DZ125 alloy at 850 °C is characterised by Stage I cracking followed by Mode I propagation, while the DD6 alloy at 1000 °C is characterised by entirely Stage I cracking. The fatal-crack initiation is primarily associated with casting pore, despite the presence of Ta, Nb and Hf-enriched blocky carbides. In terms of the higher temperatures (1000 °C for DZ125 while 1100 °C for DD6), internal oxide penetration is responsible for the Mode I cracking.
2) For the DZ125 alloy, the characteristics of Stage I followed by Mode I can be explained by the combined effect of the high-angle grain boundaries and far-field stress. When the crack length is small, the crack propagation follows the {111} slip traces in each grain, and the high misorientation angle between adjacent grains causes the crack path deflection. When the crack length becomes sufficiently large (comparable to a couple of grains), the far-field stress seems to play a predominant role, resulting in the shift from the crystallographic Stage I to Mode I propagation.
3) Test condition (i.e. temperature and duration) is the primary factor influencing the surface recrystallisation, whereas the specimen's surface condition appears to be secondary, and the formation of γ′ depletion due to oxidation may enhance recrystallisation. Although the recrystallised surface grains can introduce strain localisation in the subsurface, no evidence suggests their role on oxide penetration. This is supported by the observation that internal oxidation and associated Mode I cracks occur regardless of the surface recrystallisation.
4) The fatigue-life model predictions are within a factor of four of the experimental results obtained from the test conditions excluding DD6 1100 °C, regardless of a mixed Mode I and Mode II loading (K_{OCT}) or pure Mode I loading (and K_I) is concerned.

Data availability statement

The raw data required to reproduce these findings are available upon a reasonable request. Please directly contact the corresponding author of this paper.

CRediT authorship contribution statement

Z. Zhao: Conceptualization, Supervision, Funding acquisition. **Z. Liang:** Investigation, Writing – original draft, Formal analysis, Visualization. **Q. Li:** Investigation, Formal analysis, Visualization. **F. Zhang:** Investigation, Resources. **B. Chen:** Conceptualization, Supervision, Writing – original draft, Writing – review & editing.

Declaration of competing interest

The authors declare that they have no known competing financial interests or personal relationships that could have appeared to influence the work reported in this paper.

Acknowledgement

Zihua Zhao acknowledges financial supports by the National Natural Science Foundation of China (91860110) and the National Science and Technology Major Project of China (J2019-VI-0022-0138). Bo Chen acknowledges financial supports by the UK's Engineering and Physical Sciences Research Council, through the Early Career Fellowship Scheme EP/R043973/1.

Appendix A. Supplementary data

Supplementary data to this article can be found online at https://doi.org/10.1016/j.msea.2022.142711.

References

[1] R.J. Morrissey, P.J. Golden, Fatigue strength of a single crystal in the gigacycle regime, Int. J. Fatig. 29 (2007) 2079–2084.
[2] J.Z. Yi, C.J. Torbet, Q. Feng, T.M. Pollock, J.W. Jones, Ultrasonic fatigue of a single crystal Ni-base superalloy at 1000 °C, Mater. Sci. Eng. 443 (2007) 142–149.
[3] Z. Zhao, Q. Li, F. Zhang, W. Xu, B. Chen, Transition from internal to surface crack initiation of a single-crystal superalloy in the very-high-cycle fatigue regime at 1100 °C, Int. J. Fatig. 150 (2021) 1–14, 106343.
[4] A. Cervellon, J. Cormier, F. Mauget, Z. Hervier, Y. Nadot, Very high cycle fatigue of Ni-based single-crystal superalloys at high temperature, Metall. Mater. Trans. 49 (2018) 3938–3950.
[5] A. Cervellon, J. Cormier, F. Mauget, Z. Hervier, VHCF life evolution after microstructure degradation of a Ni-based single crystal superalloy, Int. J. Fatig. 104 (2017) 251–262.
[6] P. Lukáš, L. Kunz, M. Svoboda, High-temperature ultra-high cycle fatigue damage of notched single crystal superalloys at high mean stresses, Int. J. Fatig. 27 (2005) 1535–1540.
[7] Y. Furuya, K. Kobayashi, M. Hayakawa, M. Sakamoto, Y. Koizumi, H. Harada, High-temperature ultrasonic fatigue testing of single-crystal superalloys, Mater. Lett. 69 (2012) 1–3.
[8] A. Cervellon, L.M. Bortoluci Ormastroni, Z. Hervier, T.M. Pollock, F. Pedraza, J. Cormier, Damage mechanisms during very high cycle fatigue of a coated and grit-blasted Ni-based single-crystal superalloy, Int. J. Fatig. 142 (2021) 1–13, 105962.
[9] L.M. Bortoluci Ormastroni, L. Mataveli Suave, A. Cervellon, P. Villechaise, J. Cormier, LCF, HCF and VHCF life sensitivity to solution heat treatment of a third-generation Ni-based single crystal superalloy, Int. J. Fatig. 130 (2020) 1–16, 105247.
[10] Z. Zhao, F. Zhang, C. Dong, X. Yang, B. Chen, Initiation and early-stage growth of internal fatigue cracking under very-high-cycle fatigue regime at high temperature, Metall. Mater. Trans. 51 (2020) 1575–1592.
[11] J. Miao, T.M. Pollock, J. Wayne Jones, Crystallographic fatigue crack initiation in nickel-based superalloy René 88DT at elevated temperature, Acta Mater. 57 (2009) 5964–5974.
[12] U. Paul, P.R. Sahm, D. Goldschmidt, Inhomogeneities in single-crystal components, Mater. Sci. Eng. 173 (1993) 49–54.
[13] S. Steuer, P. Villechaise, T.M. Pollock, J. Cormier, Benefits of high gradient solidification for creep and low cycle fatigue of AM1 single crystal superalloy, Mater. Sci. Eng. 645 (2015) 109–115.
[14] E. Fleury, L. Rémy, Low cycle fatigue damage in nickel-base superalloy single crystals at elevated temperature, Mater. Sci. Eng. 167 (1993) 23–30.
[15] T.P. Gabb, J. Gayda, R.V. Miner, Orientation and temperature dependence of some mechanical properties of the single-crystal Nickel-base superalloy Rene N4: Part II. Low cycle fatigue behaviour, Metall. Trans. A 17 (1986) 497–505.
[16] H. Peng, Y. Shi, S. Gong, H. Guo, B. Chen, Microstructure, mechanical properties and cracking behaviour in a nickel-base superalloy fabricated by electron beam melting, Mater. Des. 159 (2018) 155–169.
[17] Y. Hu, L. Zhang, C. Cheng, P. Zhao, G. Guo, J. Zhao, Oxidation behaviour of the Nickel-based superalloy DZ125 at 980 C, Acta Met. Sin. 30 (2017) 857–862.
[18] B. Chen, P.E.J. Flewitt, D.J. Smith, Microstructural sensitivity of 316H austenitic stainless steel : residual stress relaxation and grain boundary fracture, Mater. Sci. Eng. 527 (2010) 7387–7399.
[19] X. Chen, M. Sakaguchi, Transition behavior from Mode I cracking to crystallographic cracking in a Ni-base single crystal superalloy, Int. J. Fatig. 132 (2020) 105400.
[20] D.W. MacLachlan, D.M. Knowles, Fatigue behaviour and lifing of two single crystal superalloys, Fatig. Fract. Eng. Mater. Struct. 24 (2001) 503–521.
[21] A.H. Sherry, R. Pilkington, The creep fracture of a single-crystal superalloy, Mater. Sci. Eng. 172 (1993) 51–61.
[22] P. Zhao, B. Chen, Z. Zheng, B. Guan, X. Zhang, S. Tu, Microstructure and texture evolution in a post-dynamic recrystallised titanium during annealing, monotonic and cyclic loading, Metall. Mater. Trans. 52 (2021) 394–412.
[23] Y. Li, D. Parfitt, P.E.J. Flewitt, X. Hou, J. Quinta de Fonseca, B. Chen, Microstructural considerations of enhanced tensile strength and mechanical constraint in a copper/stainless steel brazed joint, Mater. Sci. Eng. 796 (2020) 1–13, 139992.
[24] J. Jin, R. Gao, H. Peng, H. Guo, S. Gong, B. Chen, Rapid solidification microstructure and carbide precipitation behavior in electron beam melted high-speed steel, Metall. Mater. Trans. 51 (2020) 2411–2429.
[25] A.P. Gordon, M.D. Trexler, R.W. Neu, T.J. Sanders Jr., D.L. McDowell, Corrosion kinetics of a directionally solidified Ni-base superalloy, Acta Mater. 55 (2007) 3375–3385.
[26] H. Qi, X. Liang, S. Li, S. Yang, High-temperature oxidation behaviour of DZ125 Ni-based superalloy under tensile stress, Rare Met. (2016), https://doi.org/10.1007/s12598-016-0767-7.
[27] S. Utada, L.M. Bortoluci Ormastroni, J. Rame, P. Villechaise, J. Cormier, VHCF life of AM1 Ni-based single crystal superalloy after pre-deformation, Int. J. Fatig. 148 (2021) 1–10, 106224.
[28] C. Marsh, R. Schoell, D. Kaoumi, Environmental effect on mechanical properties of a gamma-prime strengthened nickel-based alloy: effect of the surface oxidation and formation of gamma-prime free zones, Mater. Sci. Eng. 752 (2019) 136–144.
[29] L.H. Rettberg, P.G. Callahan, B.R. Goodlet, T.M. Pollock, Rejuvenation of directionally solidified and single-crystal nickel-base superalloys, Met. Mater. Trans. A. 52 (2021) 1609–1631.
[30] M. Lamm, R.F. Singer, The effect of casting conditions on the high-cycle fatigue properties of the single-crystal nickel-base superalloy PWA 1483, Metall. Mater. Trans. 38 (2007) 1177–1183.
[31] Y. Murakami, S. Kodama, S. Konuma, Quantitative evaluation of effects of non-metallic inclusions on fatigue strength of high strength steels. I: basic fatigue mechanism and evaluation of correlation between the fatigue fracture stress and the size and location of non-metallic inclusions, Int. J. Fatig. 11 (1989) 291–298.
[32] X. Chen, M. Sakaguchi, S. Suzuki, H. Inoue, M. Okazaki, Crystal plasticity mechanism of temperature-dependent crack propagation in a single crystal nickel-based superalloy, in: Superalloys, vol. 2020, 2020, pp. 324–332.
[33] J. Litz, A. Rahmel, M. Schorr, Selective carbide oxidation and internal nitridation of the Ni-base superalloys IN738LC and IN939 in air, Oxid. Metals 30 (1988) 95–105.
[34] L. Huang, X.F. Sun, H.R. Guan, Z.Q. Hu, Oxidation behaviour of the Directionally solidified Ni-base superalloy DS951 in air, Oxid. Metals 64 (2005) 303–318.
[35] J. Reuchet, L. Remy, Fatigue oxidation interaction in a superalloy –application to life prediction in high temperature low cycle fatigue, Met. Trans. A. 14 (1983) 141–149.
[36] P. Kontis, A. Kostka, D. Raabe, B. Gault, Influence of composition and precipitation evolution on damage at grain boundaries in a crept polycrystalline Ni-based superalloy, Acta Mater. 166 (2019) 158–167.
[37] L.B. Alkmin, N. Chaia, S. Utada, J. Cormier, R. Baldan, G. Coelho, C.A. Nunes, High temperature oxidation behavior of conventional and Nb-modified MAR-M246 Ni-based superalloy, Metall. Mater. Trans. 52 (2021) 2589–2600.
[38] L.B. Alkmin, S. Utada, N. Chaia, D.A. Reis, G.C. Coelho, J. Cormier, C.A. Nunes, Creep behavior of conventional and Nb-modified as-cast MAR-M246 superalloy, Mater. Sci. Eng. 813 (2021) 1–14, 141170.
[39] L. Mataveli Suave, A.S. Munoz, A. Gaubert, G. Benoit, L. Marcin, P. Kontis, P. Villechaise, J. Cormier, Thin-wall debit in creep of DS200+Hf alloy, Met. Mater. Trans. A. 49 (2018) 4021–4028.
[40] Y. Yao, C. Xing, H. Peng, H. Guo, B. Chen, Solidification microstructure and tensile deformation mechanisms of selective electron beam melted Ni3Al-based alloy at room and elevated temperatures, Mater. Sci. Eng. 802 (2021) 1–15, 140629.
[41] K.A. Al-Jarba, G.E. Fuchs, Carbon-containing single-crystal nickel-based superalloys: segregation behavior and carbide formation, J. Occup. Med. 56 (2004) 50–55.
[42] H.E. Evans, H.Y. Li, P. Bowen, A mechanism for stress-aided grain boundary oxidation ahead of cracks, Scripta Mater. 69 (2013) 179–182.
[43] L. Viskari, M. Hörnqvist, K.L. Moore, Y. Cao, K. Stiller, Intergranular crack tip oxidation in a Ni-base superalloy, Acta Mater. 61 (2013) 3630–3639.
[44] S.D. Antolovich, S. Liu, R. Baur, Low cycle fatigue behavior of Rene 80 at elevated temperature, Met. Mater. Trans. A. 12 (1981) 473–481.
[45] J.M. Martínez-Esnaola, A. Martín-Meizoso, E.E. Affeldt, A. Bennett, M. Fuentes, High temperature fatigue in single crystal superalloys, Fatig. Fract. Eng. Mater. Struct. 20 (1997) 771–788.
[46] J.L. Malpertu, L. Remy, Influence of test parameters on the thermalmechanical fatigue behavior of a superalloy, Met. Mater. Trans. A. 21 (1990) 389–399.
[47] E. Vasseur, L. Remy, High temperature low cycle fatigue and thermalmechanical fatigue behaviour of an oxide-dispersion-strengthened nickel-base superalloy, Mater. Sci. Eng. 184 (1994) 1–15.
[48] M. Reger, L. Remy, Fatigue oxidation interaction in IN100 superalloy, Met. Trans. A. 19 (1988) 2259–2268.
[49] Z. Huang, D. Wagner, C. Bathias, P.C. Paris, Subsurface crack initiation and propagation mechanisms in gigacycle fatigue, Acta Mater. 58 (2010) 6046–6054.
[50] Q.Y. Wang, C. Bathias, N. Kawagoishi, Q. Chen, Effect of inclusion on subsurface crack initiation and gigacycle fatigue strength, Int. J. Fatig. 24 (2002) 1269–1274.
[51] N. Ranc, D. Wagner, P.C. Paris, Study of thermal effects associated with crack propagation during very high cycle fatigue tests, Acta Mater. 56 (2008) 4012–4021.
[52] D. Eylon, C.M. Pierce, Effect of microstructure on notch fatigue properties of Ti–6Al–4V, Metall. Trans. A 7 (1976) 111–121.
[53] Y. Li, X. Zhang, D. Parfitt, S. Jones, B. Chen, Characterisation of microstructure, defect and high-cycle-fatigue behaviour in a stainless steel joint processed by brazing, Mater. Char. 151 (2019) 542–552.
[54] Y. Li, L. Zhang, Y. Fei, X. Liu, M. Li, On the formation mechanisms of fine granular area (FGA) on the fracture surface for high strength steels in the VHCF regime, Int. J. Fatig. 82 (2016) 402–410.
[55] Y. Murakami, T. Nomoto, T. Ueda, Factors influencing the mechanism of superlong fatigue failure in steels, Fatig. Fract. Eng. Mater. Struct. 22 (1999) 581–590.
[56] P.A.S. Reed, X.D. Wu, I. Sinclair, Fatigue crack path prediction in UDIMET 720 Nickel-based alloy single crystals, Metall. Mater. Trans. 31 (2000) 109–123.
[57] J. Telesman, L.J. Ghosn, Fatigue crack growth behavior of pwa 1484 single crystal superalloy at elevated temperatures, in: Proc. Int. Gas Turbine Aeroengine Congr. Expo., The American Society of Mechanical Engineers ASME, Houston, 1995, pp. 1–11, https://doi.org/10.1115/95-GT-452.
[58] M. Geuffrard, L. Remy, A. Koster, Lifetime modelling of fatigue crack initiation from casting defects, in: Proc. Int. Conf, . Fract., Ottawa, 2009, pp. 1–10.
[59] A. Fatemi, D.F. Socie, A critical plane approach to multiaxial fatigue damage including out-of-phase loading, Fatig. Fract. Eng. Mater. Struct. 11 (1988) 149–165.

[60] G.M. Castelluccio, D.L. McDowell, Assessment of small fatigue crack growth driving forces in single crystals with and without slip bands, Int. J. Fract. 176 (2012) 49–64.
[61] G. Marquis, D. Socie, Long-life torsion fatigue with normal mean stresses, Fatig. Fract. Eng. Mater. Struct. 23 (2000) 293–300.
[62] China Aeronautical Materials Handbook, The Editorial Committee of China Aeronautical Materials Handbook, vol. 2, China Standard Press, Beijing, China, 2002. In Chinese.
[63] A. Cervellon, S. Hémery, P. Kürnsteiner, B. Gault, P. Kontis, J. Cormier, Crack initiation mechanisms during very high cycle fatigue of Ni-based single crystal superalloys at high temperature, Acta Mater. 188 (2020) 131–144.
[64] S.E. Stanzl-Tschegg, When do small fatigue cracks propagate and when are they arrested? Corrosion Rev. 37 (2019) 397–418.
[65] Y. Hong, C. Sun, X. Liu, A review on mechanisms and models for very-high-cycle fatigue of metallic materials, Adv. Mech. 48 (2018) 201801.